ASME Journal of Turbomachinery
Online journal at:
https://asmedigitalcollection.asme.org/turbomachinery

Particle Image Velocimetry Measurements in a High-Speed Low-Reynolds Low-Pressure Turbine Cascade

Mizuki Okada[1]
Department of Turbomachinery and Propulsion,
von Karman Institute for Fluid Dynamics,
Rhode-Saint-Genèse 1640, Belgium;
École Polytechnique de Bruxelles,
Université Libre de Bruxelles,
Bruxelles 1050, Belgium
e-mail: mizuki.okada@vki.ac.be

Loris Simonassi
Department of Turbomachinery and Propulsion,
von Karman Institute for Fluid Dynamics,
Rhode-Saint-Genèse 1640, Belgium
e-mail: loris.simonassi@avioaero.it

Gustavo Lopes
Department of Turbomachinery and Propulsion,
von Karman Institute for Fluid Dynamics,
Rhode-Saint-Genèse 1640, Belgium;
Département d'Aérospatiale et Mécanique,
Université de Liège,
Liège 4000, Belgium
e-mail: gustavo.lopes@vki.ac.be

Sergio Lavagnoli
Department of Turbomachinery and Propulsion,
von Karman Institute for Fluid Dynamics,
Rhode-Saint-Genèse 1640, Belgium
e-mail: sergio.lavagnoli@vki.ac.be

Particle image velocimetry (PIV) measurements in the blade-to-blade (B2B) plane and cascade outlet plane (COP) of a high-speed low-pressure turbine (LPT) cascade were performed at engine-representative outlet Mach number (0.70–0.95), and Reynolds number (70–120 k) under steady flow conditions. The freestream turbulence characteristics were imposed by means of a passive turbulence grid. The PIV results on the B2B plane were compared against five-hole probe (5HP) and Reynolds-averaged Navier–Stokes (RANS) computations to assess the validity of measurement and simulation techniques in the engine-relevant LPT cascade flows. The PIV captured the wake depth and width measured by the 5HP whereas the RANS displayed an overprediction of the wake Mach number deficit. The 5HP was found to impose sinewave fluctuations of the measured flow angle downstream, around three times higher than PIV. Additionally, PIV estimated turbulence intensity (TI) in the cascade, showing TI decay along a streamline. At the highest Mach number, a peak TI occurred past a shock wave. Measurements of the outlet flow field highlighted a high TI in the secondary flow region whereas high degree of anisotropy (DA) was registered in the boundary of the secondary flow and freestream regions. The contribution of the streamwise fluctuation component was found to be less than the crosswise and radial components in the freestream region. Increasing the cascade outlet Mach number, the contribution of streamwise fluctuation to the DA was observed to decrease.
[DOI: 10.1115/1.4063674]

Keywords: PIV, high-speed low-pressure turbine, linear cascade, secondary flows, transonic, low-Reynolds number, measurement techniques, turbine blade and measurement advancements

1 Introduction

The ultra-high by-pass geared turbofan (GTF) is a key-enabler engine architecture to comply with the target reduction of noise and emissions by 2050.[2] By decoupling the rotational velocity of the fan and LPT through a gearbox, the LPT stage count as well as engine weight and dimension can be reduced comparatively to a modern direct drive LPT [1].

In this engine architecture, the LPT operates at transonic exit Mach numbers (M_{out} >0.70) and low-Reynolds numbers typically encountered during cruising regime [2]. The combination of these flow conditions results in a challenging environment where compressibility interacts with the transitional boundary layer encountered in LPTs [3,4]. Experimental investigations for this range of flow conditions that can be used to validate CFD tools and improve low-order models are still scarce. As an example, these data could be used to mature turbulence models used in Reynolds-averaged Navier–Stokes (RANS) computations that still struggle to capture wake mixing, and therefore losses, accurately [5].

Investigations of LPT blading tested at engine-relevant conditions were mostly conducted by means of aerothermal probes such as multi-hole pressure probes [6–11]. The immersion of probes in transonic flow fields encountered in turbomachinery applications introduces non-negligible effects in the flow being measured [12–14] as well as the testing article [15,16]. These effects become increasingly more impactful as the Mach number of the flow field in which the probe is immersed increases [17]. Point measurements performed with aerothermal probes often characterize the flow field in terms of total and static pressure, flow angles and turbulent quantities upstream and/or downstream of the cascade being tested. Hot-wire testing in low-density transonic flows suffers from inaccuracies resultant from the measured voltage being sensitive to velocity, density, temperature, and angle fluctuations [18]. This requires specific probes and calibrations to accurately predict the turbulence intensity and degree of anisotropy (DA).

Alternatively, non-intrusive measurement techniques like particle image velocimetry (PIV) are an interesting solution to characterize

[1]Corresponding author.
[2]https://www.clean-aviation.eu/clean-sky-2/programme-overview-and-structure
Manuscript received August 16, 2023; final manuscript received September 28, 2023; published online December 14, 2023. Tech. Editor: David G. Bogard.

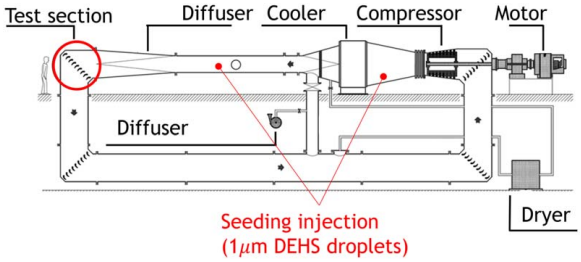

Fig. 1 S-1/C wind tunnel

the flow field in turbomachinery passages without altering its topology. The capabilities of PIV in high-speed flows are reported by Sartor et al. [19]. Another advantage compared to hot-wire testing is that turbulent quantities can be obtained independently of the density level. There are several studies dealing with PIV measurements in linear and annular turbine cascades. However, the Reynolds numbers investigated are relatively high (Re_{out} > 200 k) [20] or the outlet Mach number is subsonic (M_{out} < 0.6) [21–23]. While the experiments in subsonic flow are usually more accessible for detailed measurements in space and time, the tests do not capture the impact of compressibility. To the best of the author's knowledge, there are only a few works in open literature reporting PIV measurements in low-Reynolds transonic turbine cascades [17,24].

This work aims at extending the existing literature on PIV testing in low-density transonic turbomachinery flows. The measurements were performed in the VKI S-1/C transonic linear cascade equipped with the C1 blade exploited in the EU project SPLEEN [25,26]. The outlet Mach and Reynolds numbers were varied between 0.70–0.95 and 70−120 k, respectively.

A standard two-dimensional two-component (2D2C) PIV setup was used to characterize the Mach number in the blade-to-blade (B2B) plane. The results were compared against RANS computations. An estimation of the turbulence intensity was analyzed to verify capability of PIV as a turbulence measurement tool and to characterize the evolution of turbulence in the transonic cascade passage. The pitchwise distribution of Mach number and primary flow direction at the cascade exit extracted from B2B PIV and RANS were compared against measurements performed with a multi-directional five-hole pressure probe (5HP), a part of the open-access database[3] [27], to highlight probe induced flow modifications.

In addition, a two-dimensional three-component (2D3C) stereoscopic PIV setup was employed to characterize the flow field at the cascade outlet plane (COP) in terms of its Mach number, vorticity, and turbulent quantities. The time-averaged results were compared with the ones obtained with the multi-direction pressure probe. The comparison reinforced the challenges that arise from using intrusive probes in transonic flow fields. The turbulence field decomposed into streamwise, crosswise, and spanwise directions revealed the anisotropic turbulence distribution in both secondary flow and freestream regions.

2 Experimental Setup

2.1 Turbine Test Facility and Test Conditions. The PIV measurements were conducted in the continuously running closed-loop wind tunnel S-1/C of the von Karman Institute (Fig. 1). The wind tunnel is driven by a 615-kW 13-stage axial flow compressor. The cascade Mach and Reynolds number are independently adjusted by regulating the compressor rotational speed and the flow density inside the loop. The latter is achieved by regulating the net mass flow being removed from the loop through a vacuum pump. The flow temperature is always kept near ambient by means of a heat exchanger. The current setup enables testing at a range of Mach and Reynolds numbers ranging between 0.70 and 0.95, and 70 k and 120 k, respectively. The test conditions investigated in the scope of this work are summarized in Table 1.

Figure 2 shows a sketch of the cascade test section. A passive turbulence grid (TG) was used to reach the desired freestream turbulence intensity (TI). The freestream TI without the grid is reported to be around 0.90% [11]. Installing the TG 400 mm upstream of the central airfoil leading edge yielded a nominal TI of ∼2.4% [25]. The B2B plane measurements were conducted with and without the TG whereas the COP measurements were performed with the grid. Test case B ($Re_{out,is}$ = 70 k, $M_{out,is}$ = 0.90, with the turbulence grid) represents the nominal design point of the cascade.

2.2 Linear Cascade. The SPLEEN C1 cascade is representative of a rotor hub geometry of a geared LPT. The airfoil was designed for transonic outlet flow conditions, high deflection, and low flow acceleration. The linear cascade consists of 23 blades with a span of 165 mm. Table 2 summarizes the geometry of the tested cascade. A thorough description of the test case can be found in the study by Ref. [25].

2.3 Particle Image Velocimetry Setup. PIV Measurements were carried out in two configurations. The flow on the B2B plane at midspan was characterized by 2D2C-PIV, and the flow downstream of the cascade on the COP was investigated with stereoscopic 2D3C-PIV. The optical accesses were realized through a cascade endwall window and two sidewall windows as shown in Figs. 2 and 3. All windows were made of acrylic. For both PIV configurations, two *LaVision Imager SX 4M* cameras

Table 1 Test conditions

Test	$Re_{out,\ is}$	$M_{out,is}$	TI_{in}	PIV meas.
A	70 k	0.70	2.40%	2D2C-B2B, 2D3C-COP
B (*design*)		0.90		
C		0.95		
D	120 k	0.70		
E		0.90		
A-w/o TG	70 k	0.70	0.90%	2D2C-B2B
B-w/o TG		0.90		
C-w/o TG		0.95		
D-w/o TG	120 k	0.70		
E-w/o TG		0.90		

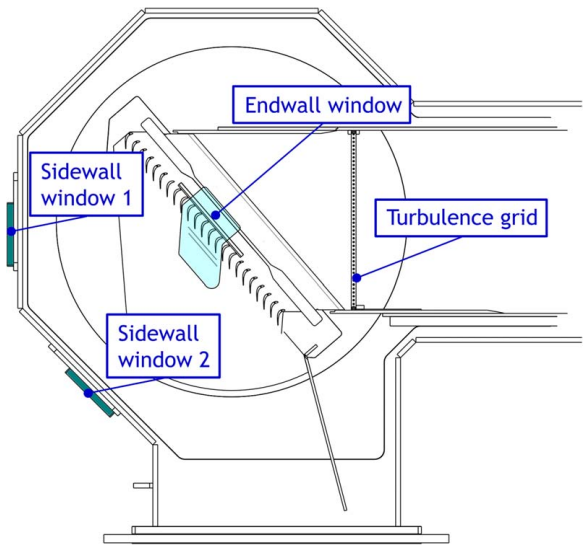

Fig. 2 Linear cascade test section

[3]https://doi.org/10.5281/zenodo.7264761

Table 2 Cascade geometry

Scaling factor	1.60	(–)
Chord, C	52.28	(mm)
Axial chord, C_{ax}	47.61	(mm)
Pitch, g	32.95	(mm)
Blade span, H	165	(mm)
Max thickness/Chord	0.127	(–)
TE thickness	0.87	(mm)
Throat opening	19.40	(mm)
Stagger angle	24.40	(deg)
Inlet metal angle, $\beta_{m,\ in}$	37.30	(deg)
Outlet metal angle, $\beta_{m,\ out}$	53.80	(deg)

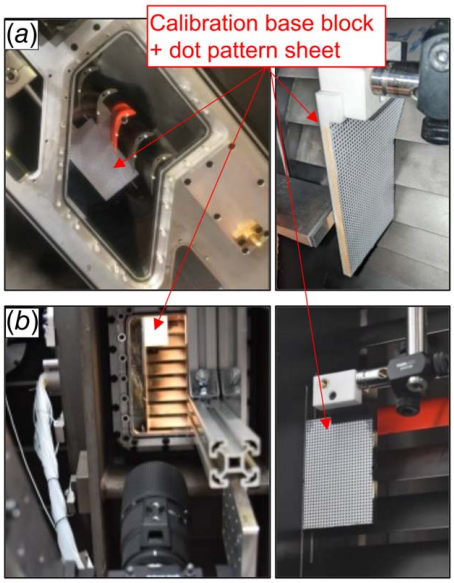

Fig. 3 Optical windows and calibration plate setups for (*a*) B2B plane measurements and (*b*) COP measurements

(2360 × 1776 pixels resolution with pixel size of 5.5 × 5.5 μm^2) and a *Litron Bernoulli PIV* laser (maximum pulse energy of 200 mJ) were used. Laskin-nozzle seeding generators *PIVTEC PIV Part 14* and *PIV Part 45* were used to produce DEHS droplets with approximately 1 μ m of diameter. The particles were seeded downstream of the wind tunnel compressor as well as upstream of the diffuser as indicated in Fig. 1, ensuring enough distance (over 5 m) to guarantee uniform seeding distribution in the test section. For each test condition, a recording of 500 double frame PIV images at an acquisition frequency of 10 Hz was repeated four times, producing 2000 PIV recordings in total. The repetition of the tests was necessary to minimize the variation of the cascade operating condition (± 3% for $Re_{out,is}$ and ± 1.5% for $M_{out,is}$) due to the seeding injection over the acquisition period.

For the 2D2C-PIV on the B2B plane, both cameras were equipped with an *AF Micro NIKKOR 60 mm f/2.8D* lens and placed side by side looking at the measurement plane through the endwall window. The laser sheet was inserted from the sidewall window 2. The field of view (FOV) of the two cameras was set to overlap by approximately 20% as shown in Fig. 4. The bottom right of the camera 2 FOV was not entirely covered by the high intensity part of the laser sheet due to the limited optical access and a need of small light sheet divergence to maintain strong enough illumination intensity for the micro-scale particle. The camera optical setup resulted in a scaling factor of about 48 pixels/mm. To reduce reflections in the recorded images, the central blade was coated with a fluorescent paint with an approximate thickness of 0.1 mm. The camera capturing the blade

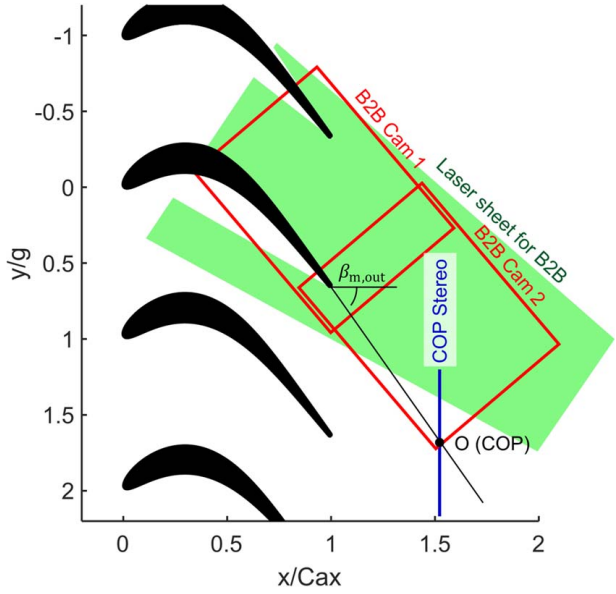

Fig. 4 FOV of the PIV measurements at B2B and cascade outlet planes

passage (Cam 1) was equipped with a 532 ± 10 nm band-pass filter to cut off the fluorescent light appears on the blade. The image calibration was performed using a laser-printed regular dot pattern sheet attached to a 3D-printed base block that fits the cascade blade passage (Fig. 3(*a*)).

For the 2D3C-PIV on the COP, one camera was equipped with a *Tamron SP AF 180 mm f/3.5 Di LD (iF) Macro* lens, and the other was equipped with a *AF Micro NIKKOR 200 mm f/4 AF-D* lens. Different lenses were used to obtain similar FOVs for different working distances. Each camera was mounted on a Scheimpflug adaptor and placed in position to observe the region of interest through the sidewall windows. The laser sheet was inserted from the cascade endwall window. The FOV covers approximately 110% of the cascade pitch (y/g) and 0–18% of the blade span (z/H). The spanwise extension of the FOV was optimized to capture the secondary flow structures at a plane that is 0.50 axial chords (C_{ax}) downstream of the blade trailing edge (TE). The FOV and COP coordinate systems are presented in Fig. 5. The setup resulted in a scaling factor of about 58 pixels/mm.

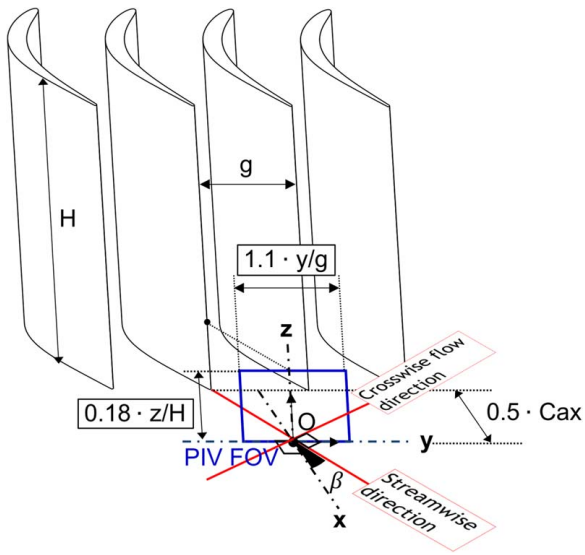

Fig. 5 Coordinate system at the cascade outlet plane

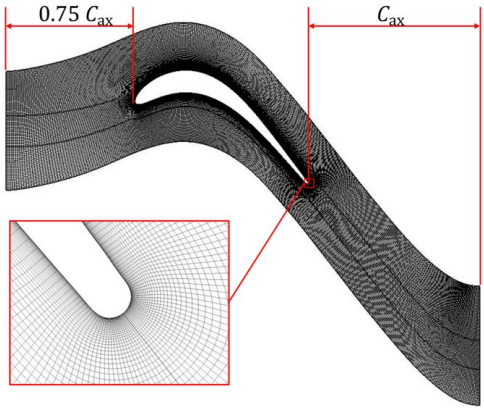

Fig. 6 Simulation domain and mesh closeup

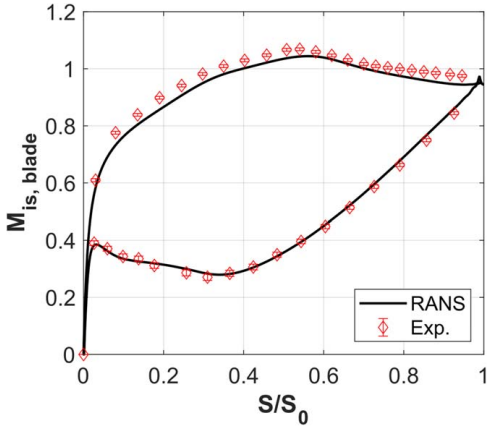

Fig. 7 Isentropic Mach number distribution on the blade, RANS versus Exp

To reduce reflections in the raw images, the blades and the bottom endwall were coated with a matte-black paint. The image calibration was performed using a laser-printed 2D calibration target consisting of a regular dot pattern as shown in Fig. 3(*b*). To reconstruct the 3D flow, the target plate was translated in the plane-normal direction, and calibration images were acquired at five equidistant positions spaced 0.5 mm apart.

Prior to the vector field computation, subtraction of the time-mean image and particle intensity normalization have been applied to reduce background and reflection noises. A case-dependent filter length varying between 11 and 51 images was used for the time-mean subtraction due to the image-to-image variation of noise pattern. The vector fields were computed using *Davis 8.4* multi-pass correlation algorithm with a starting and final interrogation window size of 128×128 pixels and 32×32 pixels with 50% overlaps. This setting resulted in vector spatial resolutions of 0.35 mm for the B2B measurement plane and 0.25 mm for the COP measurements. A spatial median filter and allowable vector ranges based on the velocity magnitude, the flow direction, and the standard deviation were employed to evaluate the validity of the computed vector. Furthermore, the local uncertainty of particle displacement deduced from correlation statistics [28] was used to remove unreliable vectors. The vectors that have the correlation-statistics-based uncertainty larger than 10% of the reference velocity speed (the isentropic outlet flow speed) have been discarded.

2.4 Midspan 2D RANS Setup. 2D Steady RANS computations were used for comparison against the results of the B2B plane PIV measurements. A structured mesh adopting O4H topology as shown in Fig. 6 was generated using *Cadence Autogrid5*. The numerical domain was extended 0.75 C_{ax} upstream of the leading edge (LE) and 1.00 C_{ax} downstream of the TE to avoid boundary reflections. The pitchwise domain size was set to be equal to the cascade pitch and periodic boundary conditions were set. The first cell height at the wall was imposed to satisfy $y^+ < 1$ to correctly resolve the viscous sub-layer. The domain was discretized with ~100 k cells. The boundary conditions were set by imposing total pressure at the inlet, static pressure at the outlet, total temperature, inlet flow angle and an inlet turbulence decay profile to match the experimental conditions in terms of Mach and Reynolds number, turbulence intensity, and length scale. Steady-state simulations were performed using *Cadence Fine/Turbo* solver adopting the $k-\omega SST$ turbulence model coupled with the $\gamma - \mathrm{Re}_{\theta t}$ transition [29]. Figure 7 presents the predicted blade isentropic Mach number distributions against the experimental data described in the study Refs. [25,26]. The experimental distributions are in good agreement with the RANS computations. The small discrepancy observed in the SS is due to the limited capability of the RANS to model the low-pressure gradient separation, recirculation, strong streamline curvature, transition, and re-laminarization [30].

2.5 Particle Traceability. The ability of a particle to trace the flow depends on various properties of the particle, the fluid, and their motions. An essential parameter for the evaluation of particle dynamics is the particle Reynolds number $\mathrm{Re}_p = \rho |V_p - V_f| d_p / \mu$, where ρ and μ are the density and viscosity of flow medium and d_p is the diameter of particle. For the estimation of Re_p, the velocity gap between the particle and the fluid $V_p - V_f$ (slip velocity) is required. Since particles are seeded far upstream of the test section and the cascade inlet flow is steady and subsonic, particles are assumed to be transported by the flow leading to the test section inlet. Near the cascade, the particles start to experience acceleration or deceleration, thus introducing slip velocity. The largest slip velocity can be caused by a shock wave potentially occurring in the blade passage for the high-Mach number test condition.

For the range of operating conditions, a maximum local Mach number in the blade passage of 1.20 is expected from the RANS computations and previous detailed measurements. For this Mach number, the largest possible velocity jump over the shock is around 94 m/s according to normal shock relations. Taking this velocity change as the maximum slip velocity, the particle Reynolds number is calculated to be 0.41. As $\mathrm{Re}_p < 1$, it is reasonable to use the Stokes' drag law to describe the particle motion in the flow; thus, the motion of particle is described by Eq. (1)

$$m_p \frac{dV_p}{dt} = 3\pi\mu d_p (V_p - V_f) \tag{1}$$

where m_p is the mass of the particle. An estimation of the velocity response through the shock for particles with diameter of 1 and

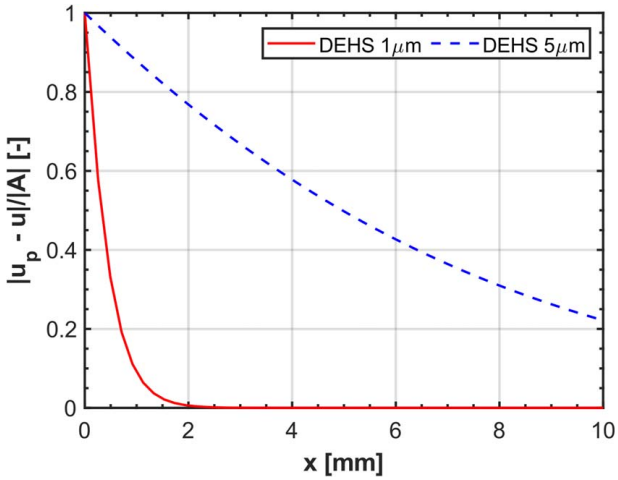

Fig. 8 Particle response through a shock

5 μ m is plotted in Fig. 8. An approximate distance of 2 mm is required for a 1 μ m particle to reach 95% of the post-shock flow velocity.

Although the particle slip can be reasonably assumed small at all instants, the integrated effect of such small drift is significant and results in undesired seeding distributions. Figure 9(*a*) displays the particle concentration predicted by a one-way coupling Lagrangian particle tracking simulation based on the 2D RANS simulations. The particle size is set to 1 μm. The concentration is normalized by the inlet particle concentration. Figures 9(*b*) and 9(*c*) show the frequency of particle occurrence obtained from the count of a sum of pre-processed 500 PIV images. The image preprocessing consists of time-series background subtraction, spatial Gaussian sliding average subtraction and max-min filter. Additionally, particle intensity normalization was applied to the raw images before the summation. The black area indicates a high probability of particle presence in the PIV recording. Note that the black areas near the blade surface are an artifact from the light reflection on the metallic airfoil. Both the simulation and the image recordings are reported for the design operating condition ($M_{out,is} = 0.90$ and $Re_{out,is} = 70$ k with TG). The red and blue lines depart from the same location, upstream of the blade leading edge, represent the streamline of the fluid (air) and the trajectory of the seeding particle, respectively. Loss of particles near the blade suction side and in the airfoil wake is observed in the PIV recordings, and the particle tracking simulation closely predicts the experimental seeding distribution. The experimental datasets have also shown that the extension of the unseeded regions grows with an increment of the Mach number and with a reduction of the Reynolds number. This trend was also confirmed by particle tracking simulations performed at the same cascade operating regimes. Kahler [31], and Bitter and Niehuis [24] reported the loss of seeding in the boundary layer of an airfoil due to the combined effect of a centrifugal force and a shear flow around the highly curved surface of the airfoil. Similarly, the core of strong vortices in high-speed flows may suffer from a significant loss of seeding.

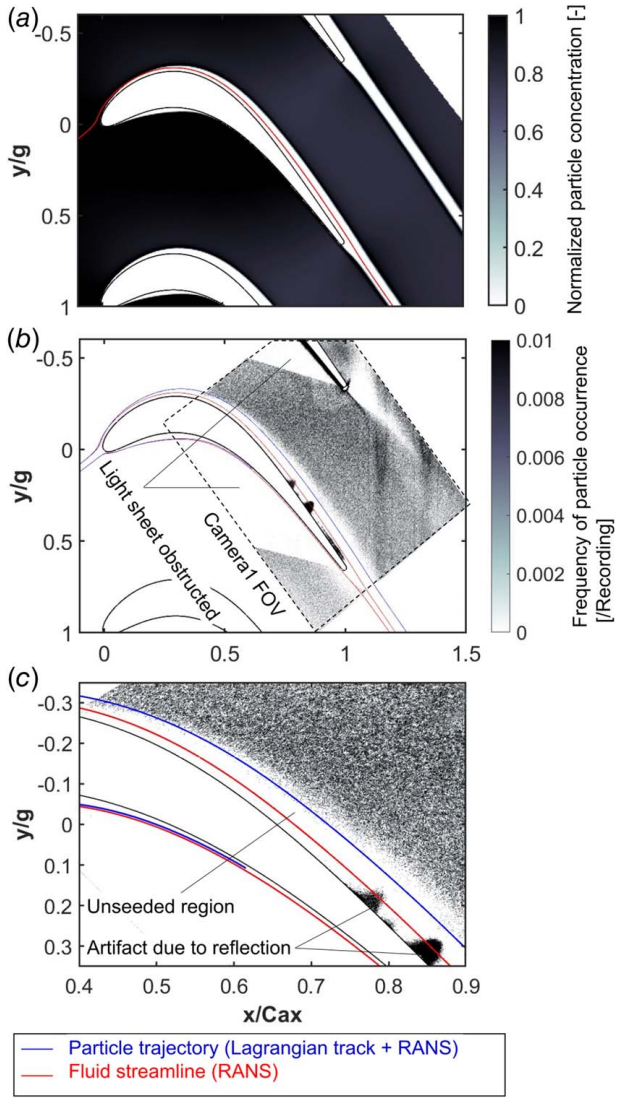

Fig. 9 (*a*) Normalized particle concentration predicted by the Lagrangian particle tracking, and (*b*) frequency of particle occurrence over 500 PIV snapshots of camera 1, and (*c*) a closeup view of (*b*) subfigure.

3 Results and Discussion

3.1 Convergence and Uncertainty of Mean Velocities.

Figure 10 shows the convergence histories of the mean velocity magnitude for the design point. Subfigures (*a*) and (*b*) present the data from the B2B plane and COP measurements, respectively. The data are sampled at four different locations, P1 and P2 are positioned in the freestream, whereas P3 and P4 sample the blade wake, as indicated in the figures in the result section. The solid lines present the ratio of the 95% confidence interval to the mean value whereas the dotted lines illustrate the root-mean-square (RMS) of the velocity fluctuations.

In both the B2B plane and the COP, the 95% CI levels at all sampling locations converge to below 1% of the mean after 500 image pair samples and to 0.5% over 2000 samples. In terms of RMS, the convergence is achieved after sampling 1000 recordings, when the

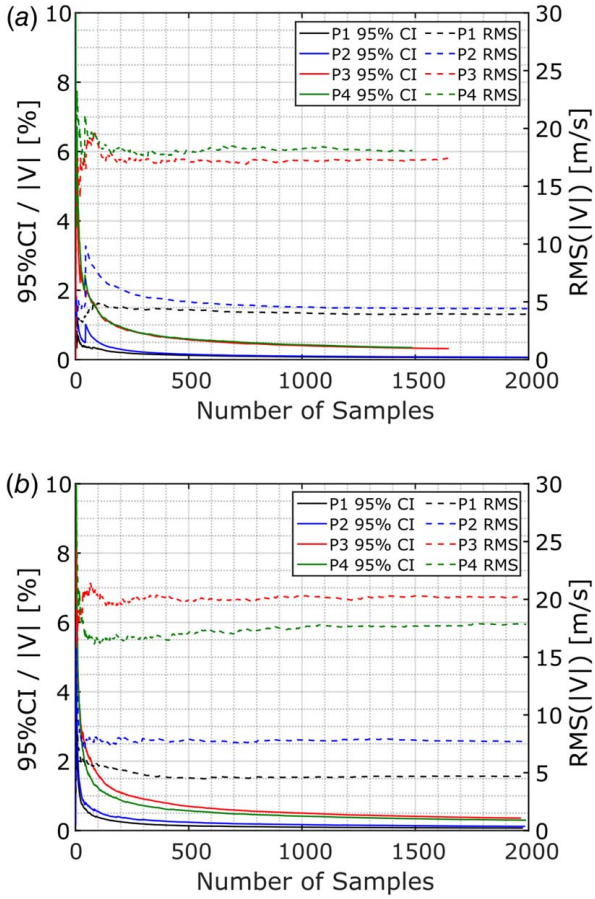

Fig. 10 Convergence histories of 95% CI and RMS of mean velocity magnitude: (*a*) B2B plane and (*b*) COP

variation of RMS stays below 2 m/s at P1 and P2. The higher level of RMS observed at the locations P3 and P4 indicates the flow unsteadiness in the blade wake. Moreover, the total number of valid samples is reduced in P3 and P4 because a larger fraction of velocity vectors at these locations were eliminated by the outlier filtering. Most of the outliers in the blade wake were found in the vortex cores due to the loss of particles. This implies that the mean computed value in the wake can be biased to the values measured outside the vortex cores. Nonetheless, the reduced number of samples is still satisfactory to achieve converged RMS.

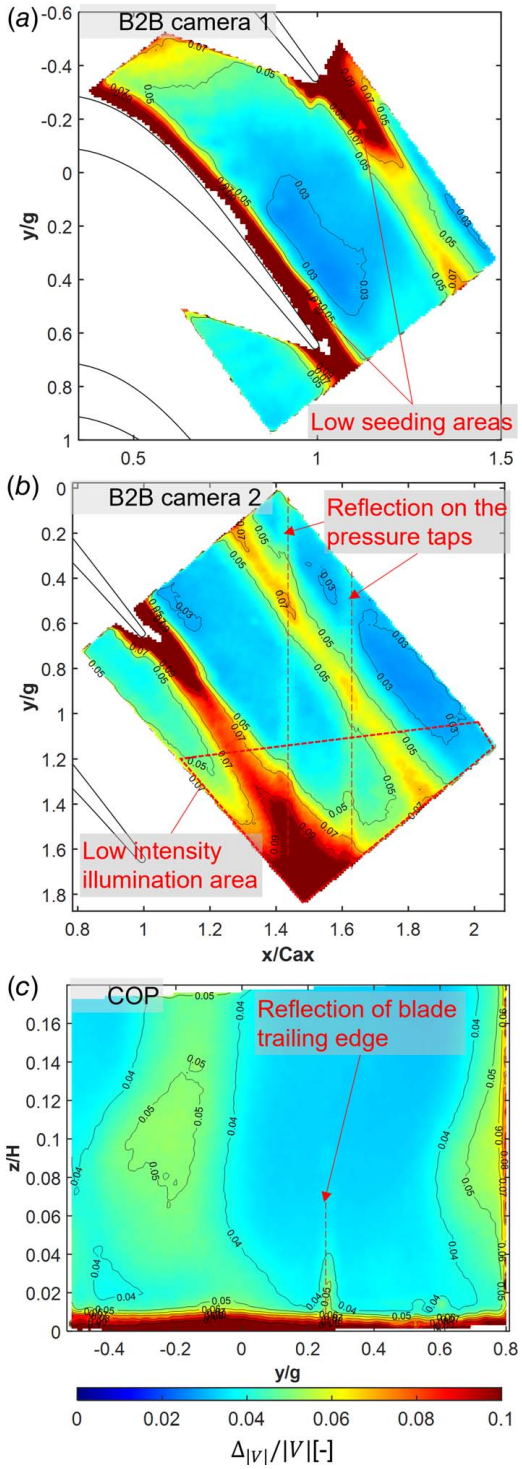

Fig. 11 Combined local uncertainty of mean velocity magnitude normalized by the local mean velocity magnitude

Uncertainty quantification in PIV measurements is particularly challenging since it is affected by numerous parameters: the setup of the optical system and its calibration, seeding quality, flow velocity gradients, and data reduction techniques. For this study, the accountable error sources are considered as follows. The systematic uncertainty ΔV_{sys} is evaluated based on the differential method proposed by Kline and McKlintock [32]

$$\Delta V_{sys} = \sqrt{\left(\frac{\partial V}{\partial \mathrm{Mag}}\right)^2 \Delta \mathrm{Mag}^2 + \left(\frac{\partial V}{\partial X_{dspl}}\right)^2 \Delta X_{dspl}^2 + \left(\frac{\partial V}{\partial t_{sep}}\right)^2 \Delta t_{sep}^2} \tag{2}$$

The uncertainty of the magnification, ΔMag, was estimated according to Ref. [33], accounting for the potential misalignment of the calibration plate (±0.5 mm in translation and ± 1 degree in rotation with respect to the laser sheet location) and for the dot pattern print resolution (0.025 mm). The pixel displacement uncertainty, ΔX_{dspl}, is estimated based on the correlation statistics [28]. The uncertainty on the separation time is 10 ns taken from the time resolution of the PIV system synchronizer (*LaVision PTU 9 sequencer*). The random uncertainty ΔV_{rand} was estimated at each final interrogation window by taking the standard deviation of 2000 PIV recordings

$$\Delta V_{rand} = \sigma_V / \sqrt{N} \tag{3}$$

The expanded combined uncertainty with a 95% confidence interval (CI) was estimated by

$$\Delta V_{combined} = 1.96 \sqrt{\Delta V_{sys}^2 + \Delta V_{rand}^2} \tag{4}$$

Figure 11 illustrates the local expanded combined uncertainty of the mean velocity magnitude computed from (*a*, *b*) B2B plane and (c) COP PIV measurements at the design test condition. The values are normalized by the local mean velocity magnitude. The values are below 5% in most of the inviscid flow regions. The outlet flow angle carries a similar uncertainty distribution, ranging up to 2.5 deg in the inviscid flow regions. The higher uncertainty observed in the region near the blade suction surface and near the blade trailing edge in the B2B plane is due to the intense light reflection and the low seeding concentration. The regions where the combined uncertainty exceeds 10% correspond to the low seeding concentration areas indicated in Fig. 9.

On the other hand, the high level of uncertainty seen in the bottom of camera 2 FOV (y/g > 1.2) is caused by the low intensity of the illumination as sketched in Fig. 4. The two vertical lines indicate the location where pressure taps were instrumented on the cascade endwall. In this area, the endwall was not painted black therefore noisier background image was observed. This resulted in a slightly higher level compared to the surroundings. Moreover, a highly turbulent swirling flow impacts negatively the uncertainty, as seen in the vortex shedding street in the B2B plane measurements and the secondary flow region of the COP. In these regions, the uncertainty is evaluated to be 1.5–2.0 times higher than in the mainstream due to the deteriorated correlation statistics and the increment of standard deviation.

3.22 Blade-to-Blade Mean Flow Field. The local Mach number can be calculated from the velocity field using the cascade inlet total temperature:

$$M = \sqrt{\frac{V^2}{\gamma R T_0 - \frac{\gamma - 1}{2} V^2}} \tag{5}$$

Figure 12 shows the Mach number contours on the B2B plane for $M_{out,is} = 0.70$, 0.90, and 0.95 while maintaining $Re_{out,is} = 70$ k for the configuration with TG. The PIV and CFD results are displayed in the top and bottom rows, respectively. The PIV fields from the

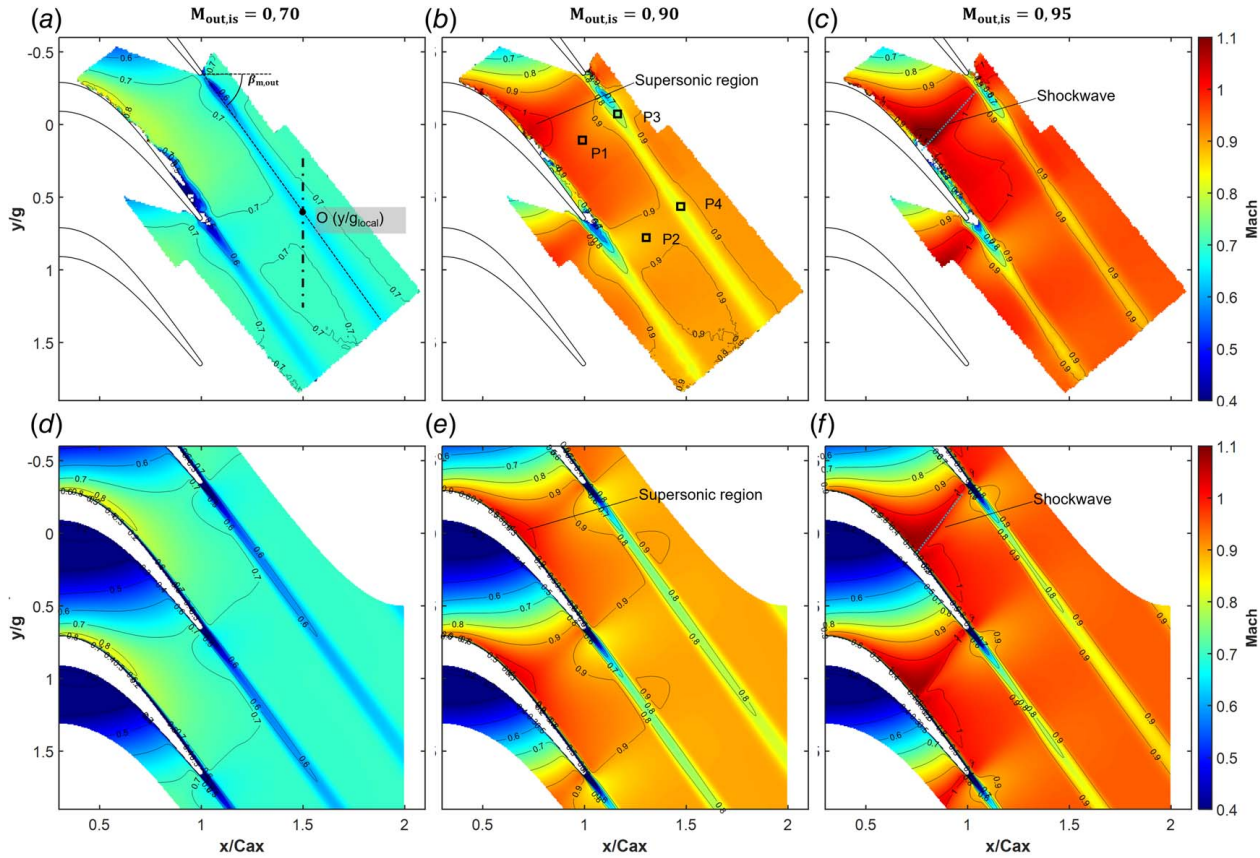

Fig. 12 Mach number fields at $Re_{out,is} = 70$ k and (*a*,*d*) $M_{out,is} = 0.70$, (*b*,*e*) 0.90, and (*c*,*f*) 0.95 from PIV and RANS

two cameras were stitched together to provide a single velocity dataset. The comparison shows a good match between PIV and RANS. The targeted outlet Mach number was reached in the downstream inviscid region (outside of the airfoil wakes). While the flow topology at different test conditions is well resolved in the center of the passage, the suction side boundary layer as well as the near-trailing edge wake could not be properly resolved due to low seeding concentrations in these regions. For the exit Mach number of 0.90, the presence of a triangle-shaped supersonic region near the throat is visible in both PIV and RANS. By increasing the Mach number to 0.95, the cascade becomes choked as the supersonic region grows, and it interacts with the adjacent blade. In the wake region, PIV measures higher flow velocity compared to RANS. This might be partially due to the bias effect of particle loss in the vortex cores.

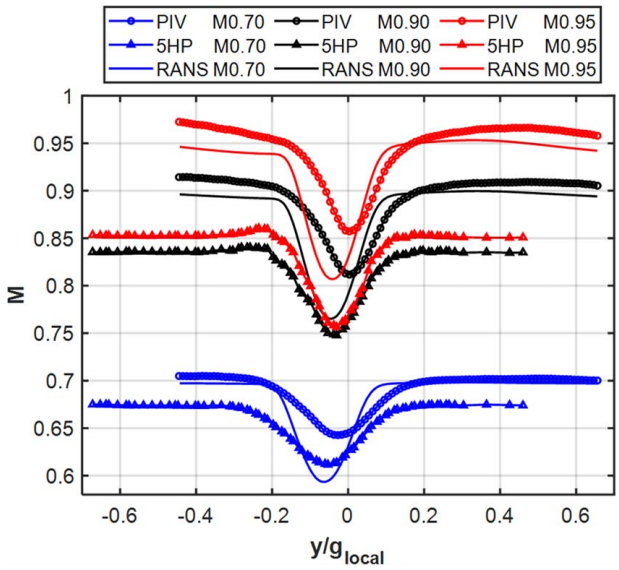

Fig. 13 Pitchwise distribution of absolute Mach number at cascade outlet from PIV, 5HP, and RANS

Figure 13 compares the pitchwise distributions of absolute Mach number at $0.50C_{ax}$ downstream of the blade TE plane retrieved from the PIV measurements (circle marker), five-hole probe (5HP) measurements (triangle marker), and RANS (solid line). Distributions for three different Mach numbers (0.70, 0.90, and 0.95) at a fixed Reynolds number of $Re_{out,is} = 70$ k are displayed. The extraction location is indicated by the dotted line in Fig. 12 (*a*—PIV). The 5HP measurements are part of the work performed by Lopes et al. [26] on the characterization of the steady aerodynamics of the SPLEEN cascade C1 at on- and off-design conditions. The total expanded uncertainty of the Mach number and deviation from the primary flow direction from the 5HP measurements were estimated to be ± 0.005 and $\pm$ 0.42 deg (20:1), respectively.

The freestream Mach number measured with PIV and computed with the RANS display good agreement for the lowest Mach number investigated. Increasing the Mach number widens the offset between the PIV and RANS, with the PIV displaying higher values than the latter.

On the other hand, the Mach number measured by the 5HP is lower than the one obtained with PIV and RANS. The offset to the RANS or PIV increases from 0.025 to 0.100 as the Mach number is increased from 0.70 to 0.95. Even though the probe was calibrated at atmospheric pressure and was used at a lower one, the Reynolds number based on the probe diameter is still sufficiently high ($Re_{probe} = 3000$) to rule out the effect of the Reynolds number [34]. The discrepancy is attributed to a probe blockage effect that forces the redistribution of mass flow to passages not

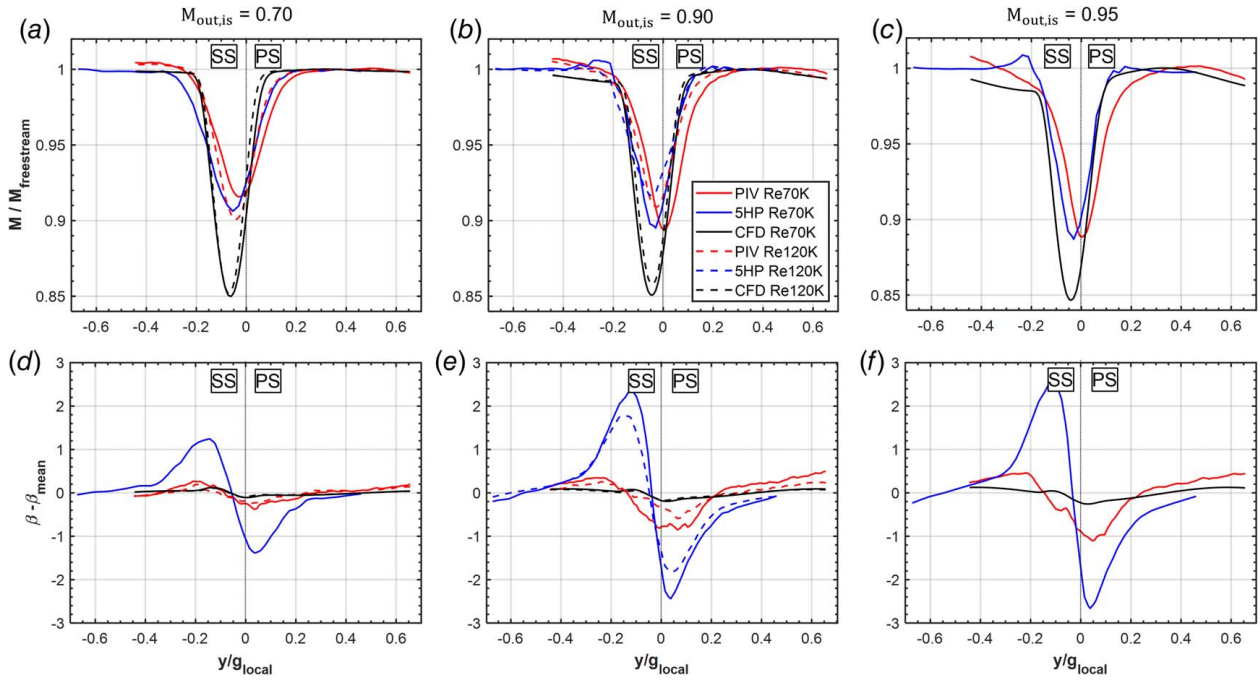

Fig. 14 Profiles of Mach number and primary flow angle (β) for the outlet Mach numbers of 0.7, 0.9, and 0.95 and Reynolds numbers of 70 K and 120 K. The profiles are extracted at 0.5 C_{ax} downstream of the blade TE.

being blocked by the probe. This causes a local reduction of the static pressure in the passage being measured by the 5HP while the total pressure is nearly unaltered. This effect was also observed by Boerner et al. [17] and Sanders et al. [35]. Lopes et al. [16] characterized this effect at different locations of the cascade: upstream, downstream, and on the blade SS.

Figures 14(*a*)–14(*c*) compare the pitchwise distributions of Mach number normalized by their own freestream values to compensate for the offsets found between the 5HP and PIV or RANS results presented in Fig 13. The wake depth measured by the 5HP and PIV are in good agreement despite the issues in retrieving static pressure with the 5HP. The difference in the wake velocity deficit is within 1% of the mean value. The wake width is also in good agreement between both techniques. The PIV results display wake misalignment, and the shift is systematic and amounts to 0.05 y/g between all the investigated cases. The error of the measurement position between the PIV and 5HP is estimated to be around 0.015 y/g (0.5 mm).

On the other hand, a large discrepancy between the RANS and experiments takes place. RANS predicted larger Mach number deficits by as much as 6% in the wake compared to the measurements. The thinner and deeper wake is attributed to turbulence models used in RANS struggling to accurately predict wake mixing when compared with higher-order methods [5,36]. At $M_{out,is} = 0.7$, both measurements and RANS present symmetric profiles, while increasing the Mach, the distribution is modulated, and an asymmetry appears. At $M_{out,\ is} = 0.95$, the 5HP measured an overshoot on the suction side (SS) edge of the wake and RANS predicted a lower freestream level on the SS.

Figures 14(*d*)–14(*f*) display the pitchwise distributions of the difference in the primary flow direction, $\beta = \tan(V_{axi}/V_{tan})$ in respect to the mean value. The PIV results present angle oscillations that are contained within ± 1 deg. On the other hand, the 5HP displays sinewave oscillations around the wake center that are caused by the probe head blockage and interaction with the blade wake. Torre et al. [14] have recently quantified this effect in a numerical setup. The distributions obtained with PIV present a reduction of the flow direction in the wake. However, no positive bump as seen in the SS for the 5HP results is observed. As the Mach number is increased, the amplitudes of the wake patterns grow, from 1.2 to 2.8 deg in the 5HP, from 0.2 to 1.0 deg in the PIV, and 0.1 to 0.4 deg in the RANS results, respectively.

Even though the tap spatial displacement of the 5HP head has been accounted for according to the first correction proposed by Ligrani et al. [37], the velocity gradient correction was not applied. Chernoray and Hjärne [38] highlighted that the first correction provides the largest difference to the uncorrected results. On the other hand, Torre et al. [14] found that even with the application of the complete correction, an underprediction of the transversal velocity components can lead to a discrepancy of 1 deg between the corrected and undisturbed values.

3.33 Blade-to-Blade Turbulence Intensity. Figure 15 presents the two-dimensional two-component turbulence intensity TI_{2C} on the B2B plane measured by PIV. Subfigure (*f*) displays the FOV of camera 1 only since the image quality of camera 2 was not satisfactory to be presented. The turbulence intensity associated with each velocity component TI_x is calculated from the RMS of the zero-mean instantaneous velocity components, $V_{x,i}$, normalized by the mean velocity magnitude $\bar{V}$

$$TI_x = \frac{V'_{x,\,\mathrm{RMS}}}{\bar{V}} = \sqrt{\frac{\sum_{i=1}^{N}(V_{x,i} - \overline{V_x})^2}{N-1}}/\bar{V} \tag{6}$$

The total two-dimensional two-component TI is calculated as

$$TI_{2C} = \sqrt{\frac{V'^2_{x,\,\mathrm{RMS}} + V'^2_{y,\,\mathrm{RMS}}}{2}}/\bar{V} \tag{7}$$

where N is the number of samples. Scharnowski et al. [39] reported that 1000 PIV recordings are required for a reliable turbulence-level estimation. In the presented cases, 2000 recordings were used. The particle displacement between double frames was on average 10–20 pixels, which is compatible with the value reported in the study by Scharnowski et al. [39]. Near the blade surface and in the region of the wake near the TE, the value of TI is not reliable as there are not enough valid vectors (due to the loss of particle information in this region).

Figure 16 compares distributions of (*a*) TI, (*b*) RMS of velocity fluctuation, and (*c*) velocity magnitude along the streamlines in the

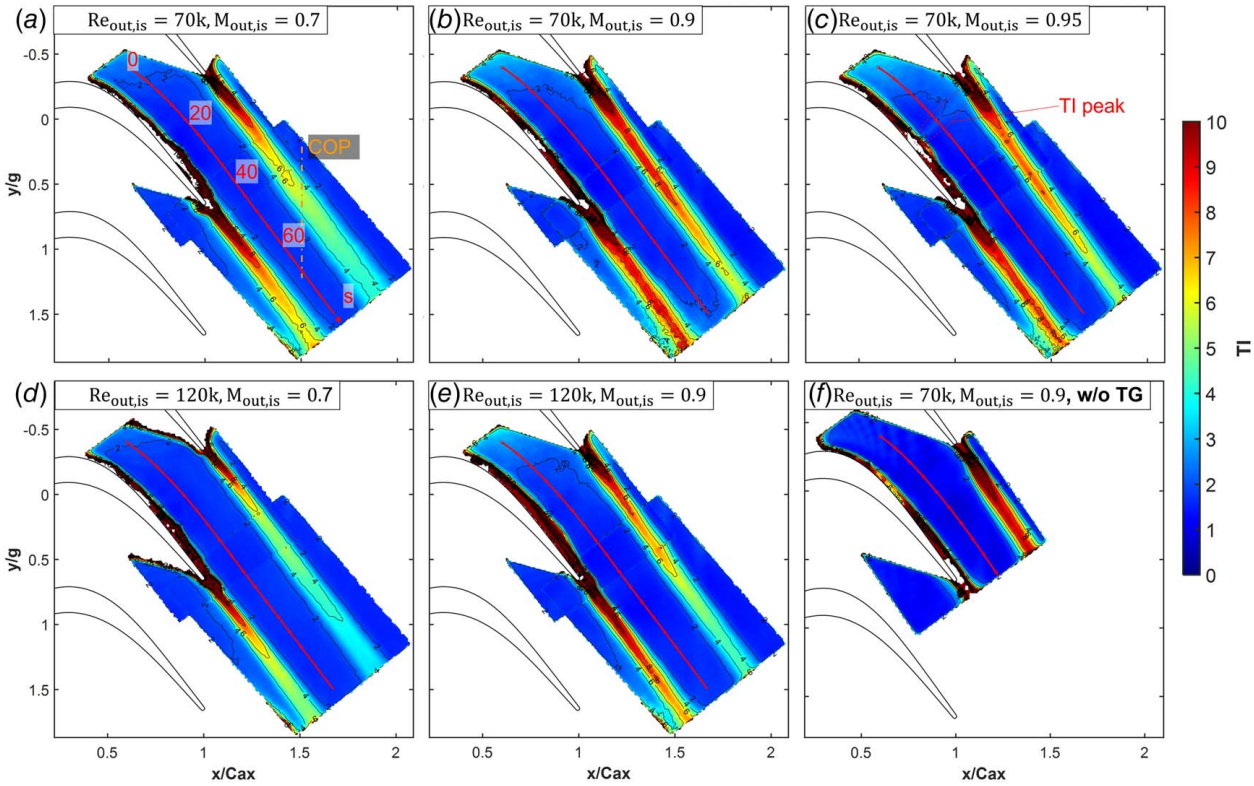

Fig. 15 Turbulence intensity at (*a*) $Re_{out,is} = 70$ k, $M_{out,is} = 0.70$ with TG, (*b*) $Re_{out,is} = 70$ k, $M_{out,is} = 0.90$ with TG, (c) $Re_{out,is} = 70$ k, $M_{out,is} = 0.95$ with TG, (*d*) $Re_{out,is} = 120$ k, $M_{out,is} = 0.70$ with TG, (*e*) $Re_{out,is} = 120$ k, $M_{out,is} = 0.90$ with TG, and (*f*) $Re_{out,is} = 70$ k, $M_{out,is} = 0.9$ without TG

freestream region indicated in Fig. 15. The horizontal axis is the path length of the streamline. Without the turbulence grid, a TI below 2% is distributed throughout the entire passage. With the turbulence grid, a TI of 1.5—3.5% upstream of the throat is found. This value decreases below 1.6% as the flow goes past the throat until the cascade exit (s = 30 mm). Such a trend is also reported in hot-wire measurements performed in a stage vane passage [40].

A similar trend is also displayed in the RMS of velocity fluctuations. On the other hand, the distribution of velocity magnitude shows a steep acceleration in the blade passage until it reaches a peak near the throat. This implies that the reduction of TI in the blade passage is due to a combination of the decay of the velocity fluctuations and the increment of the local velocity. At $M_{out,is} = 0.95$, a peak of TI appears near the throat (s = 20 mm) as seen in Figs. 15 and 16. This peak might be due to the unsteady relocation of the shock wave that increases the RMS of flow fluctuations. The peak sits in the location of the shockwave visible in Fig. 12(*c*). Lopes et al. [26] argue that a shock-boundary layer interaction occurs on the suction side of the cascade operating at $M_{out,is} = 0.95$. The onset of a laminar separation bubble was located at about 74% of the SS surface length based on surface pressure measurements. The separation onset determined by the pressure tap measurements is consistent with the impingement point of the shock wave on the blade suction side shown by the PIV results (about 72% of the SS surface length).

Figure 17 illustrates the pitchwise TI distribution extracted at $0.50C_{ax}$ downstream of the blade TE. By increasing the Reynolds number from 70 k to 120 k, the TI in the freestream region does not show significant changes whereas a reduction of about 1–2% is found in the wake region. Bitter et al. [24] reported the same trend in their PIV measurements performed at $Re_{out,is} = 60$ K and 120 K.

3.4 Cascade Outlet Secondary Flows. Figure 18 shows the contour plots of the absolute Mach number for the cases of $Re_{out,is} = 70$ k and $M_{out,is} = 0.70$, 0.90, and 0.95 measured with PIV and 5HP [26]. The horizontal (pitchwise) axis is aligned such that y/g = 0 corresponds to the intersection of the blade exit metal angle with the outlet measurement plane. Similar to the B2B measurement results, the PIV measurements confirm that the target Mach number was reached in the freestream region of the passage. On the other hand, the Mach number fields provided by the 5HP show lower values with the offset ranging from 0.05 to 0.10 as the $M_{out,is}$ is increased from 0.70 to 0.95. The underestimation of the Mach number is attributed to the probe blockage and static pressure misleading as observed in the cascade B2B measurements. The tendency of probes to underestimate the flow speed was also reported by Chemnitz and Neihuis [23] for a lower flow speed case ($M_{out,is} = 0.6$).

The topology resultant from the secondary flow structures is similar between the PIV and 5HP measurements. A region of low Mach number is visible near the endwall because of a corner vortex (CV). The horizontal dotted lines indicate the span position of local minima in the second velocity deficit region for $M_{out,is} = 0.70$. The velocity deficit region occurs at $z/H \approx 0.10$–0.12 in the PIV results. This region results from the combined effect of the passage vortex (PV) and trailing shed vortex (TSV). The 5HP displays the core to be offset by 0.01–0.02 z/H in the spanwise direction compared to the PIV.

Figure 19 presents the contour plots of the streamwise vorticity coefficient $K_{\omega,s}$ for the cases of $Re_{out,is} = 70$ k and $M_{out,is} = 0.7$, 0.9, and 0.95 measured with the PIV and the 5HP. The streamwise vorticity coefficient was computed according to the method of Gregory-Smith et al. [41] and employing the normalization reported by Taremi [42]

$$K_{\omega,s} = \frac{C}{V_{out,is}}(\omega_{axi}\cos\beta_{MS} + \omega_{tan}\sin\beta_{MS}) \tag{8}$$

where C is the blade chord length, $V_{out,is}$ is the isentropic outlet flow speed, and β_{MS} is the primary flow direction at midspan. The axial

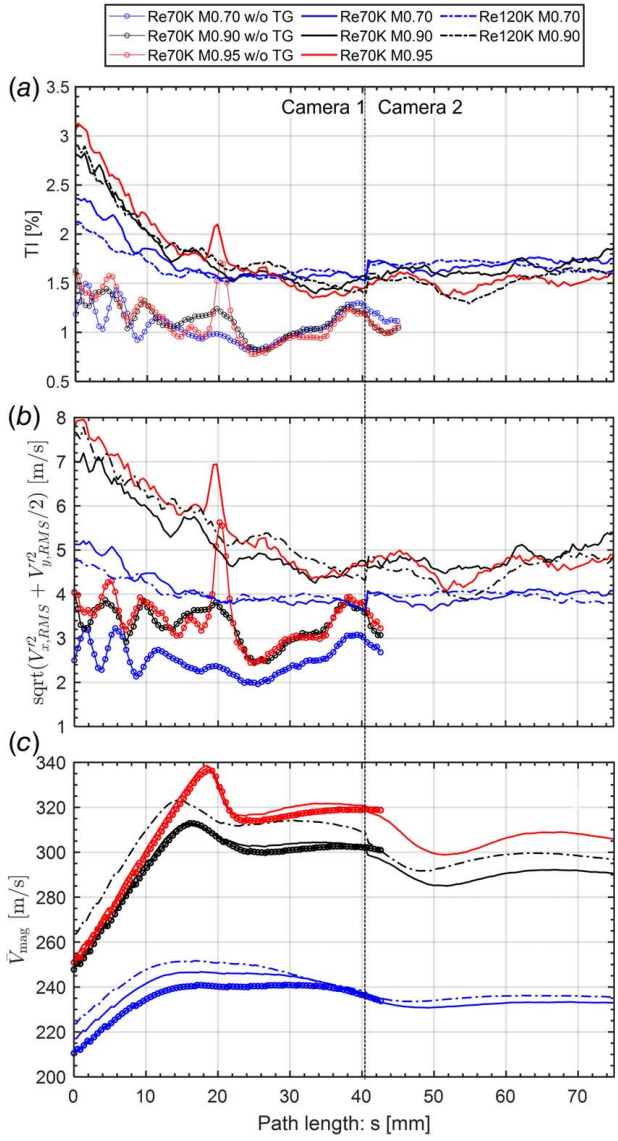

Fig. 16 Distributions of (*a*) turbulence intensity, (*b*) RMS of velocity fluctuation, and (c) velocity magnitude along the streamline plotted in Fig. 15

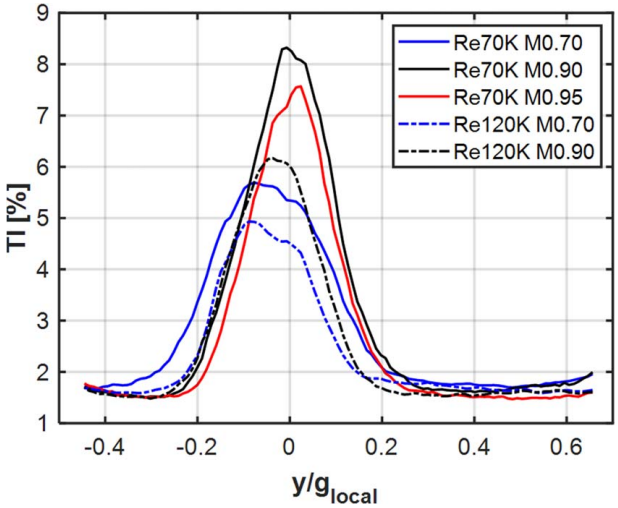

Fig. 17 Pitchwise distribution of turbulence intensity at 0.50C_{ax} downstream of the blade TE

vorticity ω_{axi} is directly computed from the COP PIV data using Eq. (9) whereas the tangential vorticity ω_{tan} is estimated using the Crocco relation (Eq. (10)) as suggested in Ref. [42]. The total pressure gradient at the outlet measurement plane, $\partial(\ln P_{0,out})/\partial z$, was taken from the 5HP measurements

$$\omega_{axi} = \frac{\partial V_{rad}}{\partial y} - \frac{\partial V_{tan}}{\partial z} \tag{9}$$

$$\omega_{tan} = \frac{1}{V_{axi}}\left(V_{tan}\omega_{axi} + \frac{a^2}{\gamma}\frac{\partial(\ln P_{0,\,out})}{\partial z}\right) \tag{10}$$

The streamwise vorticity field highlights the previously mentioned secondary flow structures: corner vortex (CV), passage vortex (PV), and trailing shed vortex (TSV). Overall, the PIV results present a lower level of streamwise vorticity than the one measured by the 5HP which can be explained by the results of the primary flow direction reported in Fig. 14 where the 5HP measured higher flow angles than the PIV. On the other hand, the evolution of the vortical structures intensity and size with the increase of Mach number is highly similar. The horizontal dot lines in Fig. 19 indicate the local minima in the TSV region for $M_{out,is} = 0.70$. As the Mach number is increased, the TSV shifts toward the endwall by about 1.5% of the blade span. Such a phenomenon is reported from 5HP measurements in the same cascade setup by Lopes et al. [26]. The latter work reported a shift of the loss peak associated with the secondary flow structures by 0.90% of the blade span as the outlet Mach number increased from 0.70 to 0.95.

Figure 20 shows the TI field for the cases of $Re_{out,is} = 70$ k and $M_{out,is} = 0.70$, 0.90, and 0.95 measured with the PIV. The TI of each velocity component and the total three-component TI are computed using Eqs. (6) and (11), respectively. The streamwise velocity V_{str} and the crosswise velocity V_{crs} were obtained with Eqs. (12) and (13)

$$TI_{3C} = \sqrt{\frac{V'^2_{x,\,RMS} + V'^2_{y,\,RMS} + V'^2_{z,\,RMS}}{3}}/\bar{V} \tag{11}$$

$$V_{str} = V_{axi}\cos\beta_{MS} + V_{tan}\sin\beta_{MS} \tag{12}$$

$$V_{crs} = V_{tan}\cos\beta_{MS} - V_{axi}\sin\beta_{MS} \tag{13}$$

High levels of turbulence are clearly observed in the secondary flow region. Regions of high streamwise and crosswise turbulent intensities are found in correspondence with the blade wake along the cascade span. A core of high turbulence intensity in the radial direction is associated with the interaction of the PV with the TSV.

The highest TI of 12% is found in the secondary flow region dominated by the crosswise flow component near the endwall. The lowest level is registered in the clean 2D freestream region where the TI of all components is lower than 6%. The turbulence components measured by Chemnitz and Neihuis [23] using a hot-wire probe and PIV in a high-subsonic Mach number ($M_{out,is} = 0.6$) flow also showed that all three components have high turbulent fluctuation spots in the wake. The reported maximum TI of 13–15% in the secondary flow region matches the presented value in Fig. 20. However, the highest value occurred in the streamwise component instead of the crosswise component.

Figure 21 illustrates the symmetric degree of anisotropy (DA_{sym}) defined by Eq. (14) for the test cases presented in Figs. 18–20.

$$DA_{sym} = \frac{\sqrt{2\overline{V'^2_{str}}} - \sqrt{\overline{V'^2_{crs}} + \overline{V'^2_{rad}}}}{\sqrt{\overline{V'^2_{str}}}} \tag{14}$$

Unlike the degree of anisotropy (DA) proposed in Ref. [43], the DA_{sym} is zero-centered; thus, the sign of the quantity directly

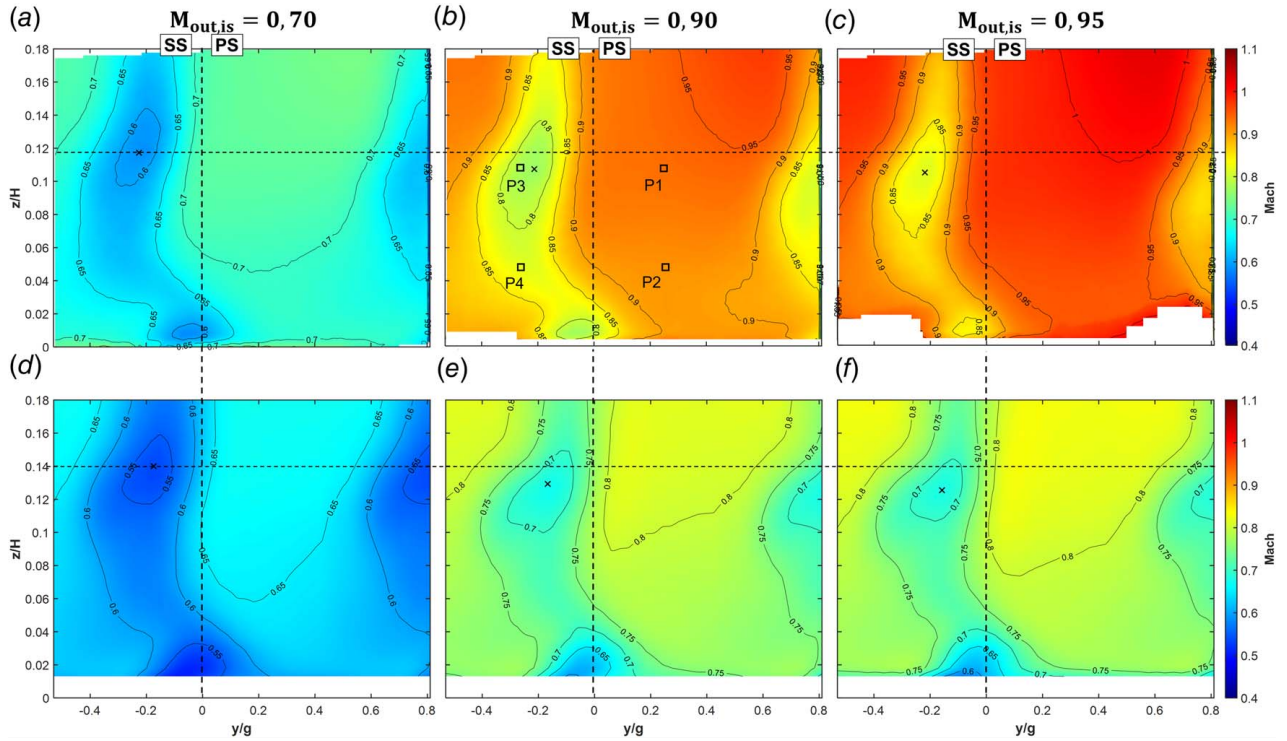

Fig. 18 Mach number fields on the COP at Re = 70 K, Ma = 0.7, 0.9, and 0.95 with TG. Top row, PIV; bottom row, 5HP.

indicates whether the turbulence field is streamwise component dominant or crosswise and radial components dominant. Positive values of the DA_{sym} are distributed on the SS region up to 50% of the cascade pitch and above 6% of the blade span. The vortical structures in Fig. 19 generate anisotropic turbulence in this region, especially at the interface of TSV with freestream or the upper part of PV. Similarly, a study of turbulence anisotropy in the flow downstream of an asymmetric airfoil showed a distribution of high DA on the SS near the boundary of the wake and freestream regions [44]. It is found that the high DA occurs in the area where shear layers are present. The anisotropic turbulence field downstream of the LPT cascade is also observed in Ref. [23].

On the other hand, the PS region up to 20–40% of the cascade pitch is characterized by the negative DA_{sym} where the contribution

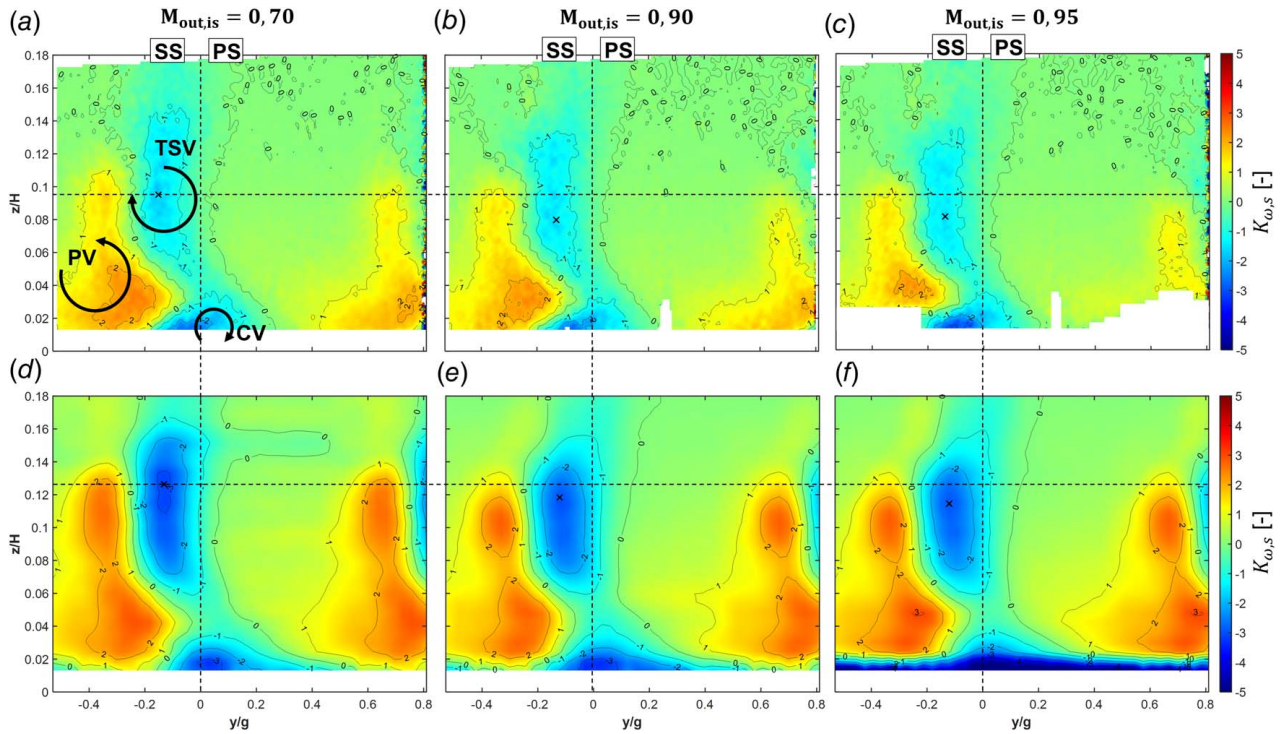

Fig. 19 Axial vorticity fields on the COP at Re = 70 K, Ma = 0.7, 0.9, and 0.95 with TG. Top row, PIV; bottom row, 5HP.

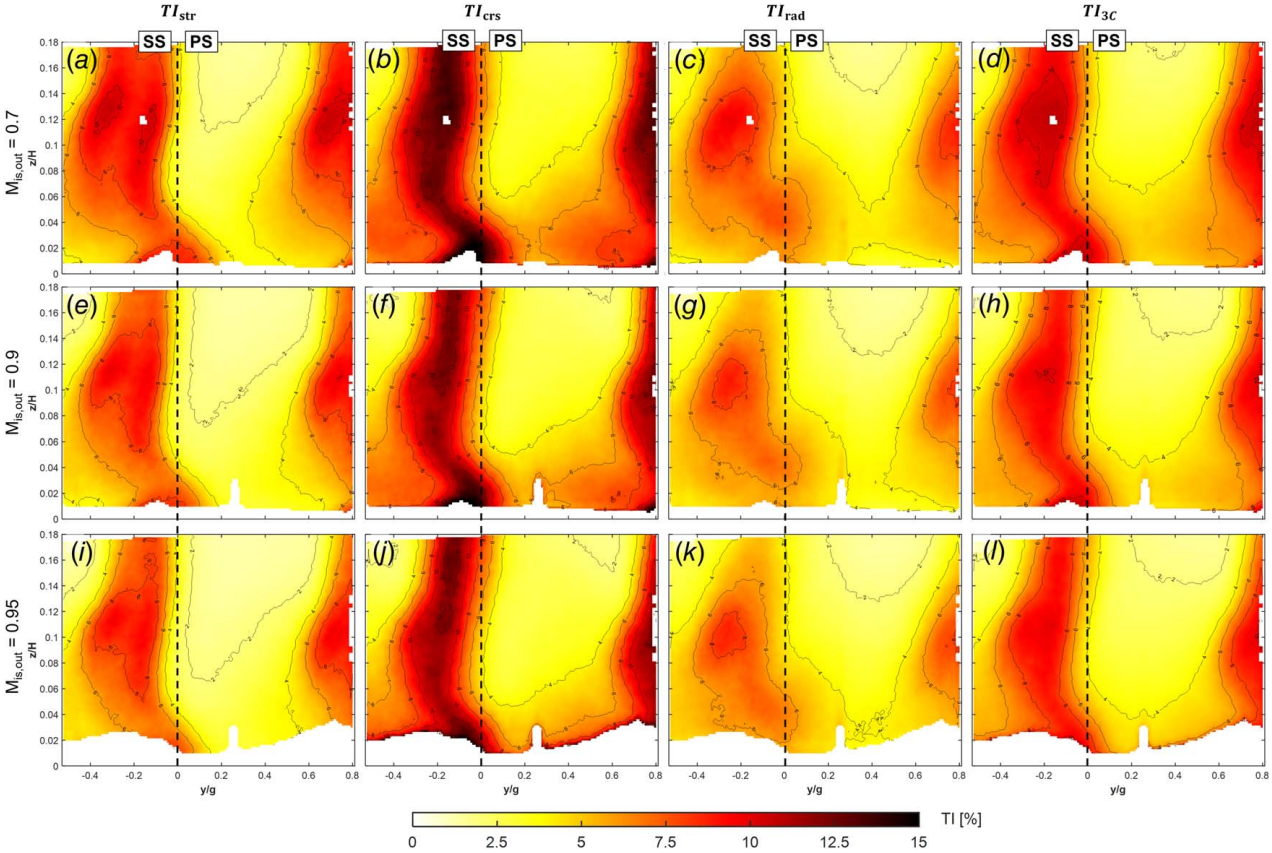

Fig. 20 Turbulence intensity on the COP at top row: Re = 70 K, middle row: Ma = 0.7, 0.9, and bottom row: 0.95 with TG

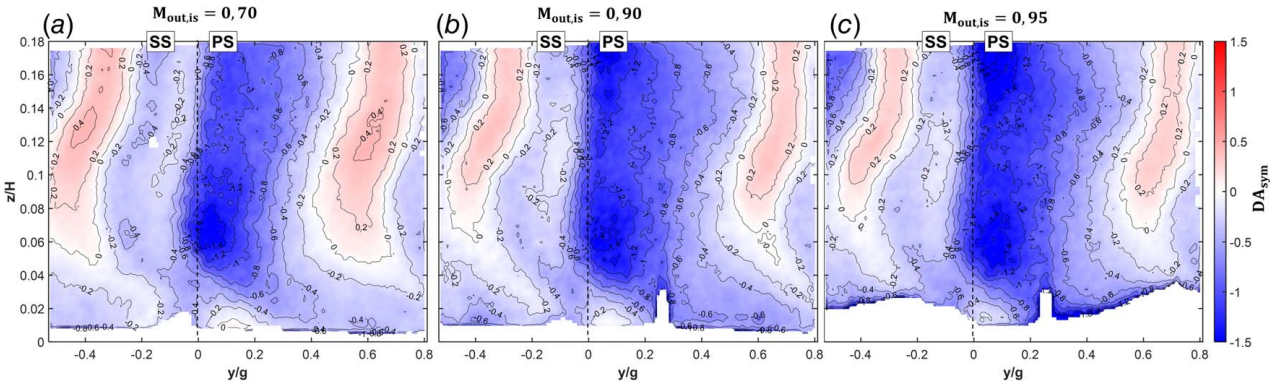

Fig. 21 Symmetric degree of anisotropy on the COP at (*a*) Re = 70 K, (*b*) Ma = 0.7, 0.9, and (*c*) 0.95 with TG

of the $\overline{V'^2_{crs}}$ and $\overline{V'^2_{rad}}$ are more pronounced than the streamwise component. A similar distribution of the DA was measured by Porreca et al. [43] using a two-sensor fast response probe downstream of the annular stator vanes. He ascribed reduced turbulence anisotropy to the stretching of the streamwise vorticity component in the uniform flow region, and a higher degree of anisotropy corresponding to the interaction of the tip passage vortex with the blade wake. Similarly, Chasoglou et al. [45] reported a DA downstream of a rotor row in the rotating frame of reference using a four-sensor fast response probe. The measured turbulence field showed a similar DA distribution with respect to the rotor wake and secondary flow structures, but with a higher level than the one measured downstream of the stator vanes.

Interestingly, the area with low DA, i.e., isotropic region, is found near the wake center and on the SS between 0–50% pitch below 5% blade span. This may imply that the turbulence components are redistributed by the interaction of strong streamwise vortical structures that enhance the flow mixing in the transverse direction.

By increasing the outlet Mach number, the turbulence intensity of all components consistently decreases and the area of negative value of DA_{sym} expands. On the other hand, the Mach number fields show that the size of the secondary flow region is maintained or even reduced. This indicates that, at a high Mach number, the stretching effect on the flow fluctuations by the freestream becomes stronger, and the effect is especially more pronounced for the streamwise component than transverse components.

These results conclude that the flow downstream of the cascade is considerably anisotropic in both secondary flow and freestream regions and the DA varies with the change of the outlet Mach number.

4 Conclusions

PIV measurements were performed in a low-Reynolds ($70\,\text{k} < \text{Re}_{\text{out,is}} < 120\,\text{k}$) and high Mach number ($0.7 < \text{M}_{\text{out,is}} < 0.95$) LPT environment. The flow field was investigated with a planar 2D2C setup for the midspan B2B plane and a stereoscopic 2D3C setup for the cascade outlet plane. For the B2B measurements, a reliable vector computation was limited to the blade main passage, due to the loss of particles in the region near the blade SS and in the wake vortex cores.

The mean isentropic Mach number fields obtained with the PIV and RANS results showed a good agreement in the topology. In addition, the presence and growth of supersonic region near the throat was observed at $\text{M}_{\text{out,is}} = 0.90$ and 0.95. A quantitative comparison between PIV, 5HP, and RANS was performed by analyzing the pitchwise distributions of the mean Mach number and primary flow direction at $0.50C_{\text{ax}}$ downstream of the cascade TE. A similar Mach number deficit in the wake with respect to the freestream is observed between PIV and 5HP, while the RANS overestimated this deficit. Different distributions of primary flow direction were obtained with the PIV, 5HP, and RANS. The PIV confirmed the intrusiveness of the 5HP on the downstream measurements where sinewave oscillations that reached as much as $\pm$ 3 deg were measured by the 5HP.

An estimation of the turbulence intensity on the B2B plane presented a decay of TI along the streamlines in the freestream region. A sharp increase in the TI past a shock wave was observed for the highest Mach number investigated. The distribution of the TI at the cascade outlet revealed the higher sensitivity of TI in the wake on the flow condition compared to the freestream region.

PIV and 5HP measurements on the COP presented a qualitatively good agreement in terms of the vortical structures present downstream of the cascade. Regions of high TI and anisotropy were found in the interfacing region of the secondary flow structures, where the shear between the secondary flow structures and freestream occurs. In the freestream region, the stochastic fluctuations in the crosswise or spanwise directions are more dominant than the streamwise components. The similarity of features of mean and turbulence flow fields with precedent studies verified the reliability of PIV measurements. The increment of the Mach number resulted in the reduced values of TI and the negative offset of DA, indicating the expansion of the freestream region.

While flow information near the blade surface and in the near blade wake was limited due to loss of particles, the PIV measurements showed promising capabilities as an investigation tool in low-Reynolds transonic LPT flows. The information of time-averaged and stochastic turbulence flow fields on the B2B and COP obtained by PIV is fruitful for the investigation of complex three-dimensional flow structure, especially in transonic flows with high-velocity gradients where intrusiveness of physical probes becomes critical for the measurement's accuracy.

Acknowledgement

The authors gratefully acknowledge funding of the SPLEEN project by the Clean Sky 2 Joint Undertaking under the European Unions Horizon 2020 research and innovation program under grant agreement 820883. The authors would also like to thank Antonino Federico Maria Torre, Davide Miglio, and Cosimo Pulieri for setting up the RANS computations, as well as Julien Desset and Gerard Goossens for supporting the modifications of the test rig and test section for optical measurements.

Conflict of Interest

There are no conflicts of interest.

Data Availability Statement

The datasets generated and supporting the findings of this article are obtainable from the corresponding author upon reasonable request.

Nomenclature

a = speed of sound
g = blade pitch (m)
m = mass (kg)
s = path length
x = axial coordinate
y = pitchwise coordinate
z = spanwise coordinate
M = Mach number
C = blade chord length (m)
H = blade span (m)
N = number of samples
R = gas constant
T = temperature
V = velocity (m/s)
d_{p} = particle diameter (m)
t_{sep} = separation time (s)
C_{ax} = blade axial chord length (m)
$K_{\omega,s}$ = streamwise vorticity coefficient
X_{dspl} = particle displacement
5HP = five-hole probe
2D2C = two-dimensional two components
2D3C = two-dimensional three components
B2B = blade-to-blade
CFD = computational fluid dynamics
CI = confidence interval
COP = cascade outlet plane
CV = corner vortex
DA = degree of anisotropy
DEHS = di-ethyl-hexyl-sebacate
FOV = field of view
GTF = geared turbofan
LDV = laser Doppler velocimetry
LPT = low-pressure turbine
Mag = optical magnification
MS = midspan
PIV = particle image velocimetry
PS = pressure side
PV = passage vortex
RANS = Reynolds-averaged Navier–Stokes
RMS = root-mean-square
Re = Reynolds number
SS = suction side
TE = trailing edge
TG = turbulence grid
TI = turbulence intensity
TSV = trailing shed vortex

Greek Symbols

β = primary flow direction (deg)
γ = specific heat ratio
Δ = uncertainty
μ = dynamic viscosity (N s/m ^{2})
ρ = density (kg/m ^{3})
σ = standard deviation
ω = vorticity

References

[1] Kurzke, J., 2009, "Fundamental Differences Between Conventional and Geared Turbofans," Proceedings of the ASME Turbo Expo 2009: Power for Land, Sea, and Air. Volume 1: Aircraft Engine; Ceramics; Coal, Biomass and Alternative Fuels; Controls, Diagnostics and Instrumentation; Education; Electric Power; Awards and Honors. Orlando, FL, June 8–12. pp. 145–153.
[2] Hourmouziadis, J., 1989, *AGARD, Blading Design for Axial Turbomachines.*, Vol. 40, Advisory Group for Aerospace Research and Development, Neuilly-sur-Seine, SEE N 89-27661 22-07.
[3] Giovannini, M., Rubechini, F., Marconcini, M., Arnone, A., and Bertini, F., 2016, "Analysis of a LPT Rotor Blade for a Geared Engine: Part I—Aero-Mechanical Design and Validation," Proceedings of the ASME Turbo

Expo 2016: Turbomachinery Technical Conference and Exposition. Volume 2B: Turbomachinery. Seoul, South Korea, June 13–17, p. V02BT38A053.
[4] Malzacher, F. J., Gier, J., and Lippl, F., 2006, "Aerodesign and Testing of an Aeromechanically Highly Loaded LP Turbine," ASME. J. Turbomach., **128**(4), pp. 643–649.
[5] Marconcini, M., Pacciani, R., Arnone, A., Michelassi, V., Pichler, R., Zhao, Y., and Sandberg, R., 2019, "Large Eddy Simulation and RANS Analysis of the End-Wall Flow in a Linear Low-Pressure-Turbine Cascade—Part II: Loss Generation," ASME. J. Turbomach., **141**(5), p. 051004.
[6] Hodson, H. P., and Dominy, R. G., 1987, "The Off-Design Performance of a Low-Pressure Turbine Cascade," ASME. J. Turbomach., **109**(2), pp. 201–209.
[7] Duden, A., and Fottner, L., 1997, "Influence of Taper, Reynolds Number and Mach Number on the Secondary Flow Field of a Highly Loaded Turbine Cascade," Proc. Inst. Mech. Eng. A: J. Power Energy, **211**(4), pp. 309–320.
[8] Vera, M., Hodson, H., and Vazquez, R., 2006, "The Effect of Mach Number on LP Turbine Wake-Blade Interaction," 10th International Symposium on Unsteady Aerodynamics, Aeroacoustics and Aeroelasticity of Turbomachines, Durham, NC, Sept. 8–11.
[9] Vazquez, R., Antoranz, A., Cadrecha, D., and Armañanzas, L., 2006, "The Influence of Reynolds Number, Mach Number and Incidence Effects on Loss Production in Low Pressure Turbine Airfoils," Proceedings of the ASME Turbo Expo 2006: Power for Land, Sea, and Air. Volume 6: Turbomachinery, Parts A and B. Barcelona, Spain, May 8–11, pp. 949–960.
[10] Vázquez, R., and Torre, D., 2012, "The Effect of Mach Number on the Loss Generation of LP Turbines," Proceedings of the ASME Turbo Expo 2012: Turbine Technical Conference and Exposition. Volume 8: Turbomachinery, Parts A, B, and C. Copenhagen, Denmark, June 11–15, pp. 1131–1142.
[11] Michálek, J., Monaldi, M., and Arts, T., 2012, "Aerodynamic Performance of a Very High Lift Low Pressure Turbine Airfoil (T106C) at Low Reynolds and High Mach Number With Effect of Free Stream Turbulence Intensity," ASME. J. Turbomach., **134**(6), p. 061009.
[12] Wyler, J. S., 1975, "Probe Blockage Effects in Free Jets and Closed Tunnels," ASME. J. Eng. Power, **97**(4), pp. 509–514.
[13] Aschenbruck, J., Hauptmann, T., and Seume, J. R., 2015, "Influence of a Multi-Hole Pressure Probe on the Flow Field in Axial-Turbines," Proceedings of the 11th European Conference on Turbomachinery Fluid Dynamics & Thermodynamics., Madrid, Spain, Mar. 23–27.
[14] Torre, A. F. M., Patinios, M., Lopes, G., Simonassi, L., and Lavagnoli, S., 2023, "Vane–Probe Interactions in Transonic Flows," ASME. J. Turbomach., **145**(6), p. 061010.
[15] Truckenmüller, F., and Stetter, H., 1996, "Measurement Errors with Pneumatic Probes Behind Guide Vanes in Transonic Flow-Fields," Proceedings of the 13th Symposium on Measuring Techniques for Transonic and Supersonic Flow in Cascades and Turbomachines, Zürich, Switzerland, Oct. 24–25.
[16] Lopes, G., Simonassi, L., Torre, A. F. M., and Lavagnoli, S., 2022, "Instrumentation Interference in a Transonic Linear Cascade," Proceedings of the XXVI Symposium on Measuring Techniques in Turbomachinery, Pisa, Italy, Sept. 28–30.
[17] Boerner, M., Bitter, M., and Niehuis, R., 2018, "On the Challenge of Five-Hole-Probe Measurements at High Subsonic Mach Numbers in the Wake of Transonic Turbine Cascades," J. Glob. Power Propuls. Soc., **2**, pp. 453–464.
[18] Cukurel, B., Acarer, S., and Arts, T., 2012, "A Novel Perspective to High-Speed Cross-Hot-Wire Calibration Methodology," Exp. Fluids, **53**(4), pp. 1073–1085.
[19] Sartor, F., Gilles, L., and Reynald, B., 2012, "PIV Study on a Shock-Induced Separation in a Transonic Flow," Exp. Fluids, **53**(3), pp. 815–827.
[20] Woisetschläger, j., Mayrhofer, N., Hampel, B., Lang, H., and Sanz, W., 2003, "Laser-Optical Investigation of Turbine Wake Flow," Exp. Fluids, **34**(3), pp. 371–378.
[21] Stieger, R. D., Hollis, D., and Hodson, H. P., 2004, "Unsteady Surface Pressures Due to Wake-Induced Transition in a Laminar Separation Bubble on a Low-Pressure Cascade," ASME. J. Turbomach., **126**(4), pp. 544–550.
[22] Canepa, E., Lengani, D., Nilberto, A., Petronio, D., Simoni, D., Ubaldi, M., and Zunino, P., 2021, "Flow Coefficient and Reduced Frequency Effects on Wake-Boundary Layer Interaction in Highly Accelerated LPT Cascade," Int. J. Turbomach. Propuls. Power, **6**(3), p. 32.
[23] Chemnitz, S., and Niehuis, R., 2020, "A Comparison of Turbulence Levels From Particle Image Velocimetry and Constant Temperature Anemometry Downstream of a Low-Pressure Turbine Cascade at High-Speed Flow Conditions," ASME. J. Turbomach., **142**(7), p. 071008.
[24] Bitter, M., and Niehuis, R., 2019, "Effects of Periodic Inflow Turbulence on the Statistics in the Wake of a Linear LPT Cascade at Jet-Engine Relevant Test Conditions," Proceedings of the 13th International Symposium on Particle Image Velocimetry–ISPIV, Munich, Germany, July 22–24.
[25] Simonassi, L., Lopes, G., Gendebien, S., Torre, A. F. M., Patinios, M., Lavagnoli, S., Zeller, N., and Pintat, L., 2022, "An Experimental Test Case for Transonic Low-Pressure Turbines—Part I: Rig Design, Instrumentation and Experimental Methodology," Proceedings of the ASME Turbo Expo 2022: Turbomachinery Technical Conference and Exposition. Volume 10B: Turbomachinery—Axial Flow Turbine Aerodynamics; Deposition, Erosion, Fouling, and Icing; Radial Turbomachinery Aerodynamics. Rotterdam, Netherlands, June 13–17. p. V10BT30A012. ASME.
[26] Lopes, G., Simonassi, L., Torre, A. F. M., Patinios, M., and Lavagnoli, S., 2022, "An Experimental Test Case for Transonic Low-Pressure Turbines—Part 2: Cascade Aerodynamics at On- and Off-Design Reynolds and Mach Numbers," Proceedings of the ASME Turbo Expo 2022: Turbomachinery Technical Conference and Exposition. Volume 10B: Turbomachinery—Axial Flow Turbine Aerodynamics; Deposition, Erosion, Fouling, and Icing; Radial Turbomachinery Aerodynamics. Rotterdam, Netherlands, June 13–17. p. V10BT30A027. ASME.
[27] Lavagnoli, S., Lopes, G., Simonassi, L., and Torre, A. F. M., 2022, *SPLEEN—High Speed Turbine Cascade—Test Case Database (Version v2) [Data set]*, Zenodo, Geneva, Switzerland.
[28] Wieneke, B., 2015, "PIV Uncertainty Quantification From Correlation Statistics," Meas. Sci. Technol., **26**(7), p. 074002.
[29] Menter, F. R., Langtry, R. B., Likki, S. R., Suzen, Y. B., Huang, P. G., and Völker, S., 2004, "A Correlation-Based Transition Model Using Local Variables—Part I: Model Formulation," ASME. J. Turbomach., **128**(3), pp. 413–422.
[30] Tyacke, J. C., and Tucker, P. G., 2015, "Future Use of Large Eddy Simulation in Aero-Engines," ASME. J. Turbomach., **137**(8), p. 081005.
[31] Kähler, C. J., 2009, "High Resolution Measurements by Long-Range Micro-PIV," Proceedings of VKI Lecture Series on Recent Advances in Particle Image Velocimetry, Rhode-Saint-Genèse, Belgium, Jan. 26–30.
[32] Kline, S. J., and McClintock, F. A., 1953, "Describing Uncertainties in Single-Sample Experiments," Mech. Eng., **75**(1), pp. 3–8.
[33] The Visualization Society of Japan, 2018, *Handbook of Particle Image Velocimetry*. Shuppan, Morikita.
[34] Bohn, D., 1977, "Untersuchung zweier verschiedener axialer Überschallverdichterstufen unter besonderer Berücksichtigung der Wechselwirkungen zwischen Lauf- und Leitrad," PhD thesis, RWTH Aachen University.
[35] Sanders, C., Terstegen, M., Hölle, M., Jeschke, P., Schönenborn, H., and Fröbel, T., 2017, "Numerical Studies on the Intrusive Influence of a Five-Hole Pressure Probe in a High-Speed Axial Compressor," Proceedings of the ASME Turbo Expo 2017: Turbomachinery Technical Conference and Exposition. Volume 2A: Turbomachinery. Charlotte, NC, June 26–30. p. V02AT39A009.
[36] Pacciani, R., Marconcini, M., Arnone, A., and Bertini, F., 2010, "A CFD Study of Low Reynolds Number Flow in High Lift Cascades," Proceedings of the ASME Turbo Expo 2010: Power for Land, Sea, and Air. Volume 7: Turbomachinery, Parts A, B, and C. Glasgow, UK, June 14–18. pp. 1525–1534.
[37] Ligrani, P. M., Baun, L. R., and Singer, B. A., 1989, "Spatial Resolution and Downwash Velocity Corrections for Multiple-Hole Pressure Probes in Complex Flows," Exp. Fluids, **7**(6), pp. 424–426.
[38] Chernoray, V., and Hjärne, J., 2008, "Improving the Accuracy of Multihole Probe Measurements in Velocity Gradients," Proceedings of the ASME Turbo Expo 2008: Power for Land, Sea, and Air. Volume 2: Controls, Diagnostics and Instrumentation; Cycle Innovations; Electric Power, Berlin, Germany, June 9–13. pp. 125–134.
[39] Scharnowski, S., Bross, M., and Kähler, C. J., 2019, "Accurate Turbulence Level Estimations Using PIV/PTV," Exp. Fluids, **60**(1), pp. 1–12.
[40] Bangert, B. A., Kohli, A., Sauer, J. H., and Thole, K. A., 1997, "High Freestream Turbulence Simulation in a Scaled-Up Turbine Vane Passage," Proceedings of the ASME 1997 International Gas Turbine and Aeroengine Congress and Exhibition. Volume 1: Aircraft Engine; Marine; Turbomachinery; Microturbines and Small Turbomachinery. Orlando, FL, June 2–5. p. V001T03A009.
[41] Gregory-Smith, D. G., Graves, C. P., and Walsh, J. A., 1988, "Growth of Secondary Losses and Vorticity in an Axial Turbine Cascade," ASME. J. Turbomach., **110**(1), pp. 1–8.
[42] Taremi, F., 2013, "Endwall Flows in Transonic Turbine Cascades," PhD thesis, Carleton University.
[43] Porreca, L., Hollenstein, M., Kalfas, A. I., and Abhari, R. S., 2007, "Turbulence Measurements and Analysis in a Multistage Axial Turbine," J. Propuls. Power, **23**(1), pp. 227–234.
[44] Yanovych, V., Duda, D., Uruba, V., and Antoš, P., 2021, "Anisotropy of Turbulent Flow Behind an Asymmetric Airfoil," SN Appl. Sci., **3**(885), pp. 1–16.
[45] Chasoglou, A. C., Mansour, M., Kalfas, A. I., and Abhari, R. S., 2018, "A Novel 4-Sensor Fast-Response Aerodynamic Probe for Non-Isotropic Turbulence Measurement in Turbomachinery Flows," J. Glob. Power Propuls. Soc., **2**, pp. 362–375.